

Journal of Materials Chemistry A

Materials for energy and sustainability

Accepted Manuscript

This article can be cited before page numbers have been issued, to do this please use: S. Sun, B. Wang and K. Huang, *J. Mater. Chem. A*, 2025, DOI: 10.1039/D5TA04992J.



This is an Accepted Manuscript, which has been through the Royal Society of Chemistry peer review process and has been accepted for publication.

Accepted Manuscripts are published online shortly after acceptance, before technical editing, formatting and proof reading. Using this free service, authors can make their results available to the community, in citable form, before we publish the edited article. We will replace this Accepted Manuscript with the edited and formatted Advance Article as soon as it is available.

You can find more information about Accepted Manuscripts in the [Information for Authors](#).

Please note that technical editing may introduce minor changes to the text and/or graphics, which may alter content. The journal's standard [Terms & Conditions](#) and the [Ethical guidelines](#) still apply. In no event shall the Royal Society of Chemistry be held responsible for any errors or omissions in this Accepted Manuscript or any consequences arising from the use of any information it contains.

Quantifying Electrokinetics of $\text{NaCa}_{0.6}\text{V}_6\text{O}_{16}\cdot 3\text{H}_2\text{O}$ Cathode in Aqueous Zinc-Ion Batteries with ZnSO_4 Electrolyte

*Shichen Sun, Boyu Wang, and Kevin Huang**

Department of Mechanical Engineering, University of South Carolina, SC29201, USA.

Abstract

Aqueous zinc-ion batteries (AZIBs) have been actively studied in recent years as a promising solution for next-generation stationary energy storage due to their inherent safety, low cost, and high energy density. However, their practical deployment remains hindered by the limited cycling stability of cathode materials. Overcoming this challenge requires a detailed understanding of cathodic electrokinetics and degradation mechanisms. In this study, we investigate the electrokinetic behavior of a $\text{NaCa}_{0.6}\text{V}_6\text{O}_{16}\cdot 3\text{H}_2\text{O}$ (NaCaVO) cathode in ZnSO_4 electrolyte through a combined application of the galvanostatic intermittent titration technique (GITT) and electrochemical impedance spectroscopy (EIS). For the first time, we quantify the exchange current density (i_0) and interfacial charge-transfer resistance (R_{CT}) of NaCaVO as a function of states of charge (SOCs). The results reveal that the $\text{V}^{4+} \rightleftharpoons \text{V}^{3+}$ redox reaction exhibits significantly slower kinetics than the $\text{V}^{5+} \rightleftharpoons \text{V}^{4+}$ counterpart. Further GITT-EIS studies using D_2O - ZnSO_4 electrolyte, complemented by X-ray diffraction (XRD) and X-ray photoelectron spectroscopy (XPS), indicate that the sluggish $\text{V}^{4+} \rightleftharpoons \text{V}^{3+}$ process is predominantly associated with proton insertion. Distribution of Relaxation Time (DRT) analysis correlates the increased interfacial resistance with the intermediate phase formation induced by this proton insertion. The electrokinetic insights obtained in this work fill critical knowledge gaps in AZIB research and provide a foundation for designing more durable and efficient cathode materials in the future.

Keywords: charge transfer resistance; exchange current density; vanadium redox reaction; ion insertion; passive layer.



I. Introduction

Rechargeable aqueous zinc-ion batteries (AZIBs) are an emerging class of electrochemical energy storage devices well-suited for stationary energy storage where cost-effectiveness, safety, and environmental sustainability are important considerations.¹⁻⁵ A typical AZIB consists of a high-energy-density zinc-metal anode, a layered or open-framework cathode, and a zinc-ion-conducting aqueous electrolyte - commonly a zinc salt solution.⁶⁻⁹ With Zn^{2+} and/or H^+ serving as the working ions, the electrochemical reactions at both cathode/electrolyte and anode/electrolyte interfaces are generally reversible, enabling rechargeable operation - a key advantage over conventional non-rechargeable alkaline Zn/MnO_2 batteries.¹⁰⁻¹⁴

Despite their promise, the commercial development of AZIBs faces serious challenges, particularly due to degradations associated with the cathode and its interfacial interactions with the electrolyte.¹⁵⁻¹⁷ Therefore, the advancement of AZIB technology critically hinges on the development of high-capacity, durable cathode materials, which in turn requires a thorough understanding of cathodic degradation mechanisms.^{1, 18-21} Additionally, there remains a substantial knowledge gap in the understanding of cathodic kinetics - especially those that govern the ion storage processes at various states of charge (SOCs).

To date, a major effort in aqueous zinc-ion battery (AZIB) research has been focused on engineering a stable zinc-anode/electrolyte interface to suppress the hydrogen evolution reaction (HER) at the zinc anode and mitigate zinc corrosion. Strategies such as surface coatings and electrolyte additives have been widely explored for this purpose. However, many of these additives inadvertently hinder cathodic kinetics, ultimately compromising overall battery performance despite effectively suppressing HER and reducing corrosion.^{22, 23}



In comparison, cathode-focused research has primarily centered on compositional modifications of MnO_2 - and V_2O_5 -based materials to enhance capacity and cycling stability. A notable example is the pre-insertion of alkaline and alkaline-earth metal cations into V_2O_5 -based structures.^{8, 24-29} In these studies, a variety of *in situ* and *ex situ* surface and bulk characterization techniques - such as X-Ray Diffraction (XRD), X-ray Photoelectron Spectroscopy (XPS), Electron Microscopy, Fourier Transform Infrared Spectroscopy (FTIR), and X-ray Absorption Spectroscopy (XAS) - are routinely employed to probe material properties and elucidate underlying reaction mechanisms. In parallel, conventional electrochemical techniques³⁰ such as Galvanostatic/Potentiostatic Intermittent Titration (GITT/PITT),^{31, 32} electrochemical impedance spectroscopy (EIS),³³ and cyclic voltammetry (CV)^{34, 35} are used to study electrochemical behaviors. Despite these efforts, rigorous investigation of cathodic electrokinetics during actual charge and discharge processes remains rare. Furthermore, many early studies only evaluated charge-transfer resistance (R_{CT}) under open-circuit conditions, which do not accurately represent real operating states of AZIBs, thereby limiting their value for mechanistic understanding and battery performance modeling.

In this study, we present a combined GITT and EIS approach to probe cathodic electrokinetics under actual operating conditions. The cathode material of choice is $\text{NaCa}_{0.6}\text{V}_6\text{O}_{16} \cdot 3\text{H}_2\text{O}$ (NaCaVO), previously identified in our work as a stable and promising candidate for AZIB applications with outstanding cyclability (e.g., 94% capacity retention after 2,000 cycles at 2 A/g and 83% after 10,000 cycles at 5 A/g).³⁶ Electrokinetic measurements were conducted using a three-electrode configuration, with NaCaVO as the working electrode (WE), zinc metal as the counter electrode (CE), Ag/AgCl as the reference electrode (RE), and 2 M ZnSO_4 as the electrolyte - an industry-relevant formulation. To deconvolute overlapping electrochemical processes and better interpret cathodic behavior, we also apply Distribution of Relaxation Times (DRT) analysis



to EIS spectra, correlating observed features with the formation of interfacial secondary phases. Additionally, to investigate the co-intercalation mechanisms of Zn^{2+} and H^+ into the NaCaVO structure, we employ water isotope solvent D_2O in the ZnSO_4 electrolyte system to distinguish the contributions of zinc ions from those of protons.

II. Results and Discussion

2.1. Electrokinetics quantification using combined GITT-EIS method

The cyclic voltammetry (CV) profiles of the NaCaVO cathode in 2 M H_2O - ZnSO_4 electrolyte at scan rates ranging from 0.1 to 1.0 mV/s are shown in Figure 1. Two distinct pairs of redox peaks, corresponding to the redox transitions of V-oxidation state, are consistently observed across all scan rates. The high-potential redox couple (D_1 at ~ 0.81 - 0.82 V and C_1 at ~ 0.91 - 0.93 V vs. Zn/Zn^{2+}) is assigned to the $\text{V}^{5+} \rightleftharpoons \text{V}^{4+}$ redox reaction, while the lower-potential couple (D_2 at ~ 0.56 V and C_2 at ~ 0.70 V) is related to the $\text{V}^{4+} \rightleftharpoons \text{V}^{3+}$ reaction.³⁷⁻⁴¹ With increasing scan rate, both anodic and cathodic peak currents rise systematically, indicating charge-transfer-controlled behavior. However, the lower-potential peaks (D_2/C_2) are consistently broader and exhibit smaller peak currents relative to D_1/C_1 , suggesting that the $\text{V}^{4+} \rightleftharpoons \text{V}^{3+}$ reaction proceeds with slower kinetics and greater polarization than the $\text{V}^{5+} \rightleftharpoons \text{V}^{4+}$ reaction. Moreover, the potential separation between cathodic and anodic peaks slightly widens with scan rate, particularly for the $\text{V}^{3+}/\text{V}^{4+}$ redox couple, further indicating that kinetic limitations and sluggish charge transfer dominate at low potentials. Overall, there is no significant change in redox peak position at different scan rates, justifying our use of potential to characterize electrokinetic behaviors of the $\text{V}^{5+} \rightleftharpoons \text{V}^{4+}$ and $\text{V}^{4+} \rightleftharpoons \text{V}^{3+}$ redox reactions during the charge and discharge cycles.



Moreover, to investigate the ion diffusion characteristics in the NaCaVO cathode in H₂O-ZnSO₄ system, cyclic voltammetry (CV) conducted at varying scan rates (0.1-1.0 mV/s) was further analyzed by plotting the peak currents corresponding to distinct redox reactions vs. square root of scanning rate to determine diffusion coefficient of the electroactive species of a diffusion-controlled redox process using Randles–Ševčík equation:^{42, 43}

$$I_p = (2.69 \times 10^5) \times n^{3/2} \times A \times D^{1/2} \times C \times \nu^{1/2} \quad (1)$$

Here I_p is the peak current (A), n is the number of electrons transferred, A is the electrode area (cm²), D is the diffusion coefficient (cm²/s) of the electroactive species, C is the molar concentration of electroactive species (mol/cm³), and ν is the scan rate (V/s).

Figure 1 (b) shows that a plot of I_p versus $\nu^{1/2}$ of the four redox peaks follow a linear relationship, indicating semi-infinite diffusion as the rate-limiting process. The calculated diffusion coefficients related to the four redox peaks are 4.74×10^{-10} and 1.37×10^{-10} cm²/s for C_1 and D_1 , respectively, located at the high-potential region and 1.14×10^{-11} and 3.11×10^{-11} cm²/s for C_2 and D_2 , respectively, located at the low-potential peaks. The higher D values for the high-potential V⁴⁺/V⁵⁺ redox couple than the V³⁺/V⁴⁺ counterpart suggests a facile kinetics for the former, which will be further discussed in the following sections.

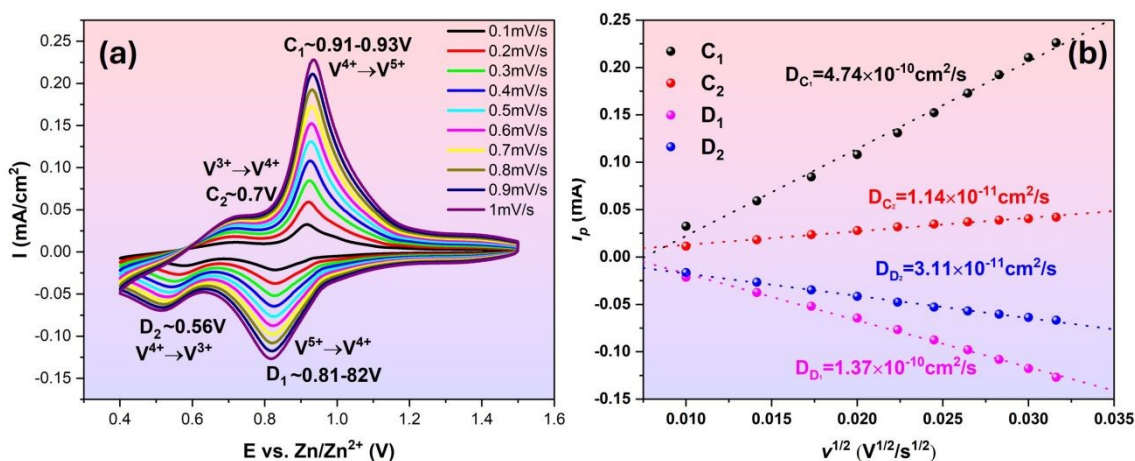


Figure 1. H_2O - ZnSO_4 system: (a) CV and (b) I_p vs. $v^{1/2}$ of $\text{NaCaVO}|2\text{M ZnSO}_4|\text{Zn}$ cell scanned at different rates. RE: Ag/AgCl; CE: Zn; WE: NaCaVO.

The potential (E) profiles collected by GITT during charge and discharge cycle are shown in Figure 2(a). As potential E increases and decreases with time during charge and discharge cycle, respectively, pseudo-plateaus regions (quasi-flat regions) show good alignment with the two redox peaks identified in the CV (see Figure 1(a)). During the charge cycle, the profile exhibits a mid-E pseudo-plateau around 0.85-0.95 V (corresponding to $\text{V}^{4+} \rightarrow \text{V}^{5+}$ oxidation peak) and a lower pseudo-plateau near 0.60-0.70 V (corresponding to $\text{V}^{3+} \rightarrow \text{V}^{4+}$ oxidation peak). Similar pseudo-plateaus are also observed during the discharge cycle, corresponding to $\text{V}^{5+} \rightarrow \text{V}^{4+}$ and $\text{V}^{4+} \rightarrow \text{V}^{3+}$ reduction peaks, respectively. The greater E changes in lower E region than in higher E region imply higher polarization and sluggish kinetics in the region.

The EIS spectra collected at each GITT step during charge and discharge cycled at ± 50 mA/g (equivalent to ± 0.024 mA/cm²) are shown in Figure 2(b) and 2(c), respectively, as an example. Each spectrum is measured under different bias currents to obtain $R_{CT}=R_{CT}(i)$ at a specific E (or SOC) created by the preceding galvanic polarization. From Figure 2(b) collected during the charging cycle, it is evident that EIS spectra feature a charge transfer impedance at high frequencies, followed by low-frequency Warburg impedance (related to semi-infinite surface diffusion of the active species) over low E range (step 1-10, 0.53-0.70 V). As E increases, the spectra gradually transit to a mixed Warburg (step 11-14, 0.72-0.78 V) and charge-transfer only feature (step 15-28, 0.80-0.93 V) over intermediate E range, and finally to charge-transfer only feature over high E range (step 29-45, 0.95-1.50 V). During the discharging cycle, the above trend remains, i.e., Warburg impedance appears at low E, whereas charge-transfer-only feature appears at high E. Note that the appearance of Warburg impedance at low E range implies diffusion



limitation to the active species; we will further correlate it with the formation of an intermediate phase in the following section. The original E vs. time profiles and corresponding EIS spectra collected under OCV and other current densities such as 75-125 mA/g can be found in Figure S1. By comparing Figure 2 and Figure S1, it is concluded that the shape of all profiles (two distinct pseudo-plateau regions) remains the same, suggesting that the electrochemical reaction mechanisms remain unchanged by the applied current.

With the equivalent circuit model shown in Figure 2(b-1), R_{CT} under low E is extracted from the interception length on Z' -axis of the fitted curve (dotted), and for the high E cases, R_{CT} (sum of R_{CT1} and R_{CT2}) is similarly taken using the equivalent circuit model in Figure 2(c-1). The obtained R_{CT} is then plotted against E and shown in Figure 3 for both charge and discharge cycle in a current range of 0-125 mA/g. A clear dependence of R_{CT} on E is observed. In both charge and discharge cycles, the R_{CT} - E profiles can be divided into three stages. **Stage-1**, the lowest E range (0.40 - 0.60 V for both charge and discharge), R_{CT} is generally the highest but decreases with E. **Stage-2**, the intermediate E range (0.68 – 0.91 V for charge and 0.60 – 0.83 V for discharge), a maximum is observed. **Stage-3**, the high E range (>0.91 V for charge and >0.83 V for discharge), a plateau is observed. The minimal R_{CT} appears to occur at a high E close to the $V^{5+} \rightleftharpoons V^{4+}$ as indicated in CV, see Figure 1. In contrast, high R_{CT} appears at lower E range close to the $V^{4+} \rightleftharpoons V^{3+}$. Therefore, we can conclude from Figure 3 that the $V^{4+} \rightleftharpoons V^{3+}$ redox reaction is more sluggish than the $V^{5+} \rightleftharpoons V^{4+}$ counterpart. This finding could be explained by a greater difficulty in inserting/extracting ions into/from NaCaVO at a deeper SOC. Another reason could be related to the formation of intermediate phase on the surface of NaCaVO cathode due to proton insertion; we will show evidence to support this assertion in a later section. On the other hand, in the higher E and shallow SOC regime, the charge transfer kinetics is facile with low R_{CT} , suggesting a lower presence of the



intermediate phase. In addition, the ohmic resistance R_0 of all cells studied was roughly $\sim 0.45 \Omega \cdot \text{cm}^2$ (see Figure 2 and S1), independent of DC bias applied.

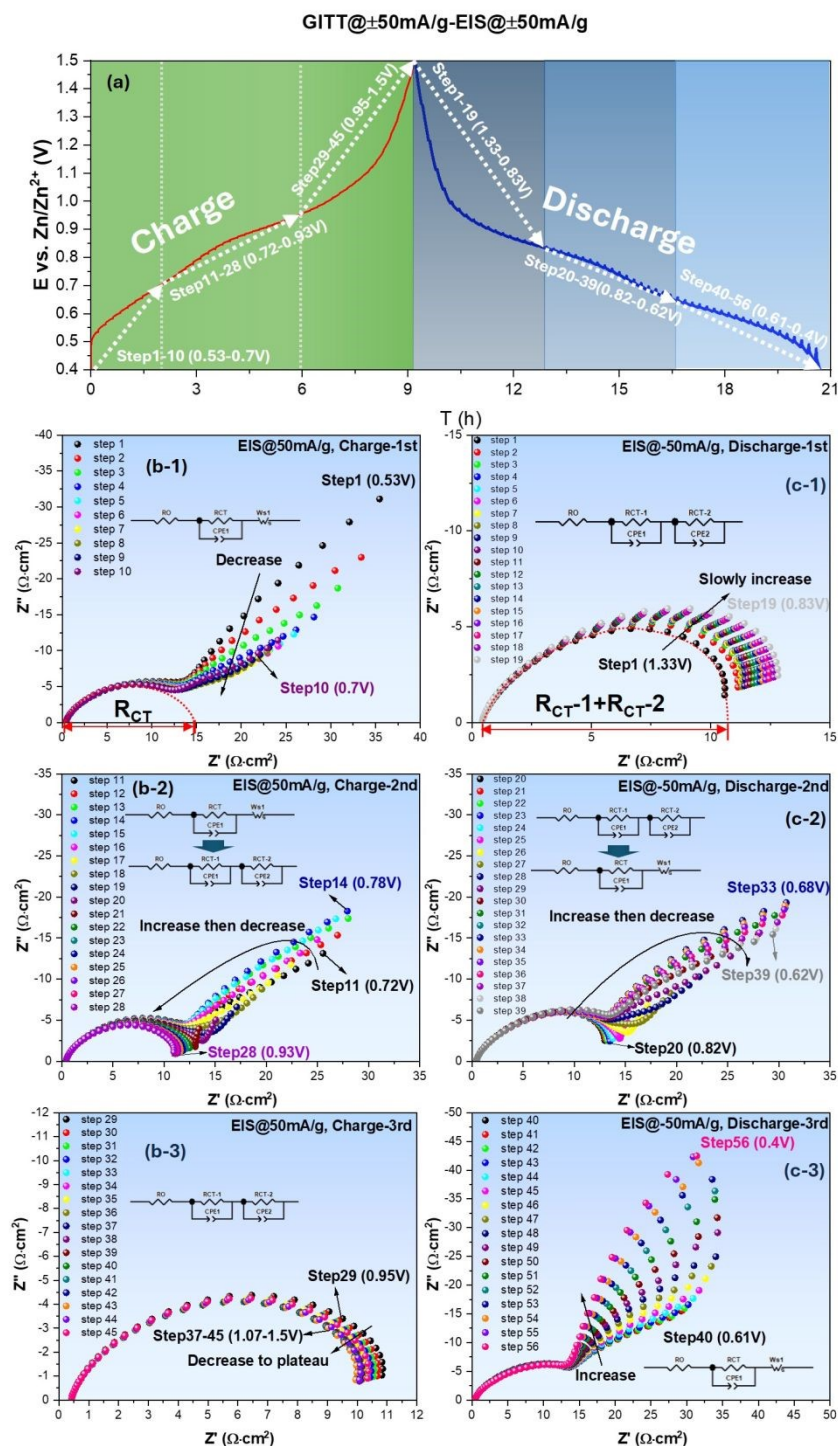


Figure 2. $\text{ZnSO}_4\text{-H}_2\text{O}$ system: (a) E vs. time profile collected under ± 50 mA/g; EIS spectra measured with ± 50 mA/g bias during charge (b) and discharge (c) cycles.

The trend of enhanced charge transfer kinetics by the applied current agrees with Butler-Volmer law that predicts higher overpotential drives a lower R_{CT} . The agreement also suggests that the charge transfer kinetics is a rate limiting step of the ion insertion process into NaCaVO. Although the shapes of two $R_{\text{CT}}\text{-}E$ profiles between charge and discharge cycle are close to a mirror image, the discharge cycle does exhibit a slightly higher R_{CT} than the charge cycle at the same E , indirectly reflecting influence of the intermediate phase formation on charge transfer process.

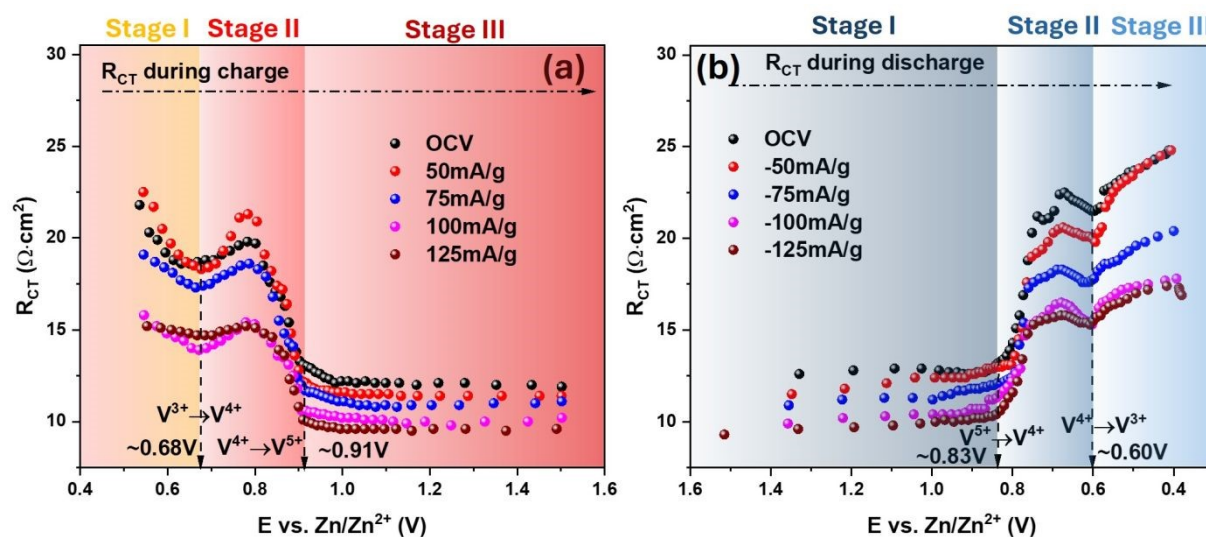


Figure 3. $\text{H}_2\text{O-ZnSO}_4$ system: R_{CT} vs. E during (a) charge and (b) discharge cycle under different current densities.

2.2. Exchange current density (i_0)

With the obtained R_{CT} vs. i , we apply the “low-field” approximation of Butler-Volmer equation to extract exchange current density (i_0), a key parameter of electrokinetics, as the current density range applied in this study generally falls into “weak polarization” regime: ⁴⁴

$$\eta = (RT/nF) * (i/i_0) \quad (2)$$



where η is the overpotential; i is the applied current density; $n=1$ is the number of electrons transferred; i_0 is the exchange current density; R and T have their usual meanings. To obtain i -dependent η , we further integrate the experimental $R_{CT}=R_{CT}(i)$ shown in Figure 4(a) and obtain η - i relationship shown in Figure 4(b). The selected potentials correspond to the regions where the charge transfer resistance (R_{CT}) reaches a minimum or forms a plateau in the R_{CT} vs. E plot (see Figure 3), specifically at ~ 0.68 V and ~ 0.91 V during the charge, and ~ 0.60 V and ~ 0.83 V during the discharge, close to those of the redox reactions of $V^{5+} \rightleftharpoons V^{4+}$ and $V^{4+} \rightleftharpoons V^{3+}$. As is shown, a linear relationship is observed with a current density up to 125 mA/g, implying that the “low-field” approximation is valid.

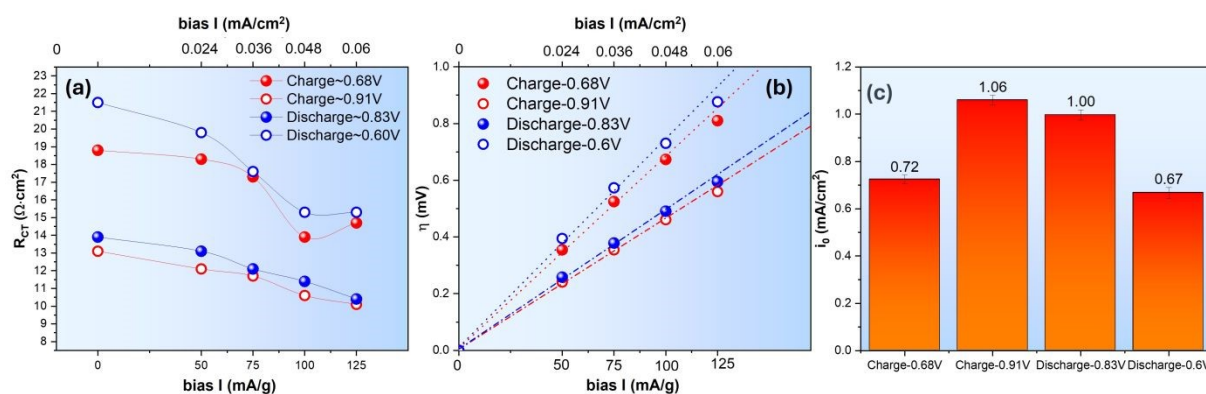


Figure 4. H_2O - $ZnSO_4$ system. (a) R_{CT} vs. i , (b) η vs. i and (c) i_0 comparison at 0.68 V and 0.91 V during charge and 0.83 V and 0.6 V during discharge.

A comparison of i_0 at different E of the charge and discharge cycle is given in Figure 4(c); it informs that i_0 is higher at higher E than at lower E . Between the charge and discharge cycle for the same pair of redox reaction, i_0 is higher for the charge cycle than the discharge cycle. Again, these comparisons suggest that the $V^{5+} \rightleftharpoons V^{4+}$ is a more facile redox reaction than the $V^{4+} \rightleftharpoons V^{3+}$ counterpart. We hypothesize that the sluggish $V^{4+} \rightleftharpoons V^{3+}$ redox reaction could be attributed to the intermediate phase formation induced by the H^+ insertion at a deeper SOC. To verify this, we



performed a further analysis on EIS spectra with DRT method and replacing of H₂O with D₂O as a solvent for the ZnSO₄ electrolyte.

2.3 Analysis of EIS spectra with DRT method

Even though our GITT-EIS method provides E-dependent R_{CT} data under different i , we still do not fully understand the reasons why the kinetics of $V^{5+} \rightleftharpoons V^{4+}$ is faster than $V^{4+} \rightleftharpoons V^{3+}$. We here apply DRT method to facilitate the understanding.⁴⁵ Figure 5 shows an exemplary contour plot of γ -function of DRT analysis over a time domain (τ , Relaxation time constant, unit in s) superposed with E (SOC) during a constant polarization at 50 mA/g, where τ is related to the frequency (f , in Hz) in EIS by:

$$\tau = \frac{1}{2\pi f} \quad (3)$$

By correlating the E vs. time profiles with the corresponding DRT contour plots, specific phase formation and deformation processes can be revealed by the emergence or suppression of the $\gamma(\ln \tau)$ response in the contour map within defined potential regions. At the peak redox potentials (see Figure 1(a)), *i.e.* 1.50 to ~0.80 V and ~0.65 to 1.50 V corresponding to the $V^{5+} \rightleftharpoons V^{4+}$ reaction during charging and discharging, respectively, while 0.40 to ~0.80 V and ~0.65 to 0.40 V corresponding to the $V^{4+} \rightleftharpoons V^{3+}$ reaction during charging and discharging, respectively, the DRT plots unveil significant impedance response. At shorter relaxation time (<0.001s, high frequency), the impedance is generally low in either charge or discharge regimes, implying that the charge transfer process of NaCaVO cathode with ZnSO₄ electrolyte is facile. At longer relaxation time (0.1-0.001 s, low frequency), the impedance is high in either charge or discharge regimes, implying possible diffusion limitation. The intermediate phase formed during the discharge process could be responsible for the high impedance at low-frequencies. In fact, the Warburg impedance tails



become steeper at higher current densities, see Figure 2 and S1, inferring an increasing diffusion resistance. The intermediate phase formed during the discharge cycle could be a reason; we will show the evidence in the following section. For all current densities (OCV, 50, 75 and 100 mA/g), Figure 5 suggest that this “intermediate phase effect” is reversible upon the charge and discharge cycle.

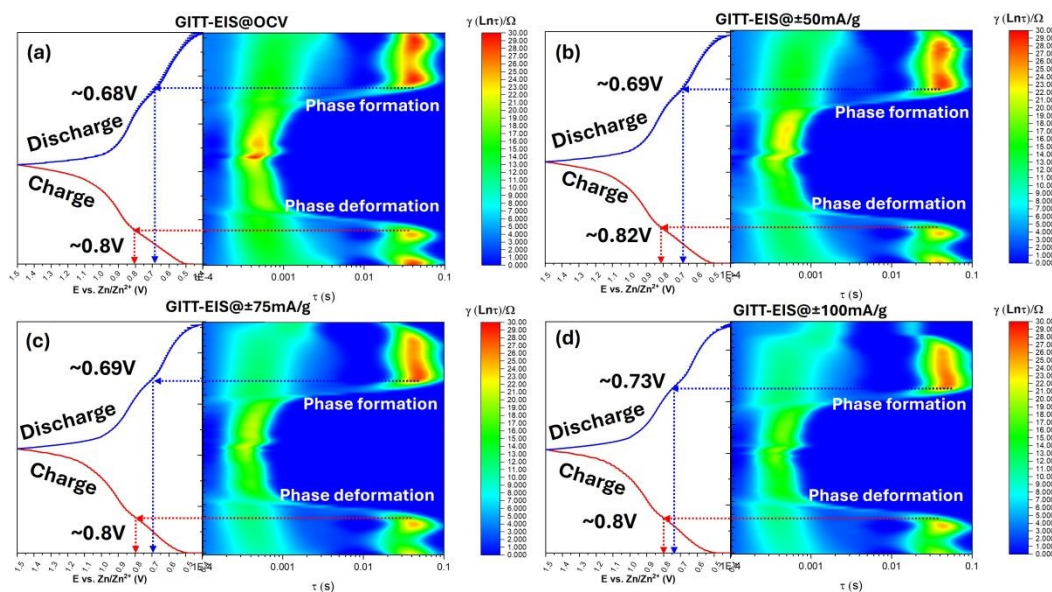


Figure 5. E vs. time profiles (left) and corresponding DRT contour plots (right) derived from EIS of the NaCaVO cathode in H_2O - ZnSO_4 electrolyte during charge-discharge cycles under (a) OCV, (b) ± 50 mA/g, (c) ± 75 mA/g, and (d) ± 100 mA/g. The DRT maps reveal phase formation and deformation processes via intensity variations in $\gamma(\ln \tau)$ across specific potential ranges.

2.4 Evidence of intermediate phase formation

To identify the composition of the secondary phase, we performed *ex-situ* XRD and XPS. Figure 6 shows XRD patterns of NaCaVO cathode after being cycled under different SOCs. From the main peak of NaCaVO in Figure 6(a), it is evident that the ion (de)insertion processes are generally reversible during the charge/discharge cycle, exhibiting lattice contraction during the discharge



due to strong Zn^{2+} - O^{2-} interactions after Zn^{2+} are inserted and lattice expansion during the charge after Zn^{2+} are extracted. More importantly, Figure 6(b) indicates that an intermediate phase with a composition of $\text{Zn}_4\text{SO}_4(\text{OH})_6 \cdot x\text{H}_2\text{O}$ (herein denoted as Zn-LDH) is detected in NaCaVO only after being cycled at low E between 0.40 and 0.80 V (related to $\text{V}^{3+} \rightleftharpoons \text{V}^{4+}$). The finding of Zn-LDH at low-E-cycled NaCaVO provide chemical reason for the slow electrokinetics of $\text{V}^{3+} \rightleftharpoons \text{V}^{4+}$ and aggravated diffusion impedance. Since it is well known to the AZIB community that Zn-LDH is a product of H^+ insertion into the cathode, it further suggests that H^+ insertion might take place at lower E. ^{46, 47} This contrasts with some theoretical calculations suggesting that H^+ insertion takes place mainly at higher E. ⁴⁸⁻⁵⁰

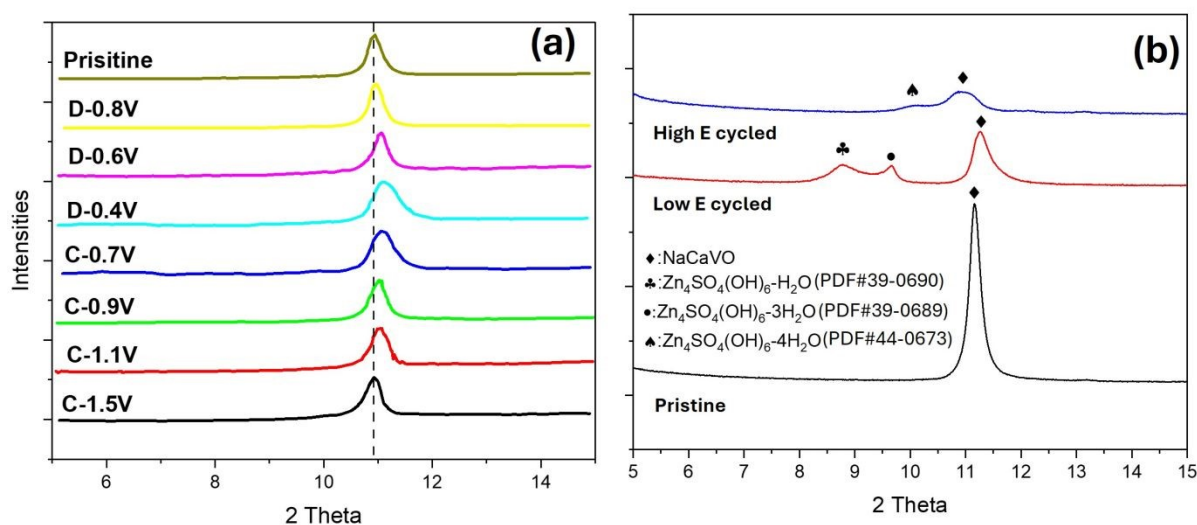


Figure 6. H_2O - ZnSO_4 system. Ex-situ XRD patterns of NaCaVO cathode after (a) charge and discharge at different SOC levels and (b) cycled at low and high E compared with the pristine.

The XPS spectra shown in Figure S4 indicate a weaker V-2p signal in NaCaVO after cycling at low E than those of the pristine and cycled at high E, suggesting possible blocking effect by the Zn-LDH formed. Furthermore, the ratio of $\text{V}^{3+}/\text{V}^{4+}$ in NaCaVO becomes significantly higher after cycling at low E compared to the pristine (with V^{5+} and trace V^{4+}) and the high-E-cycled one (with



much lower V^{3+}/V^{4+} ratio), which is consistent with our previous results.³⁶ These XPS results further suggest that the low-E redox reaction is associated with $V^{3+} \rightleftharpoons V^{4+}$ and high-E redox reaction is related to $V^{5+} \rightleftharpoons V^{4+}$.

2.5 Effect of D_2O on electrokinetics

To further verify if the H_2O -derived H^+ insertion into NaCaVO is responsible for the redox reaction of $V^{3+} \rightleftharpoons V^{4+}$, we performed the same GITT-EIS experiment using the same $ZnSO_4$ electrolyte but isotope D_2O as the solvent. Figure S2 shows the original CV curves of NaCaVO in D_2O - $ZnSO_4$, which is notably different from the H_2O - $ZnSO_4$ case, especially in the low E range (0.5 - 0.7 V). In particular, the redox peaks associated with the $V^{3+} \rightleftharpoons V^{4+}$ become less pronounced and shifted toward lower E, reflecting the impact of heavier D^+ ions on this redox reaction. The more pronounced broadening and reduced peak current density suggests a retarded reaction kinetics. These observations support the hypothesis that H^+/D^+ impacts on the $V^{3+} \rightleftharpoons V^{4+}$ redox reaction at lower E.

The E-profiles collected from the D_2O - $ZnSO_4$ system under 50 mA/g by GITT during charge and discharge cycle are shown in Figure 7 as an example; similar plots at other current densities can be found in Figure S3. The two-step pseudo-plateau feature remains, suggesting two active charge transfer processes: $V^{3+} \rightleftharpoons V^{4+}$ and $V^{4+} \rightleftharpoons V^{5+}$. However, a quick glance of EIS spectra indicate that R_{CT} at low E is appreciably higher than the H_2O - $ZnSO_4$ counterpart, inferring that the $V^{3+} \rightleftharpoons V^{4+}$ kinetics has become more sluggish by the slower D^+ (de)insertion process.



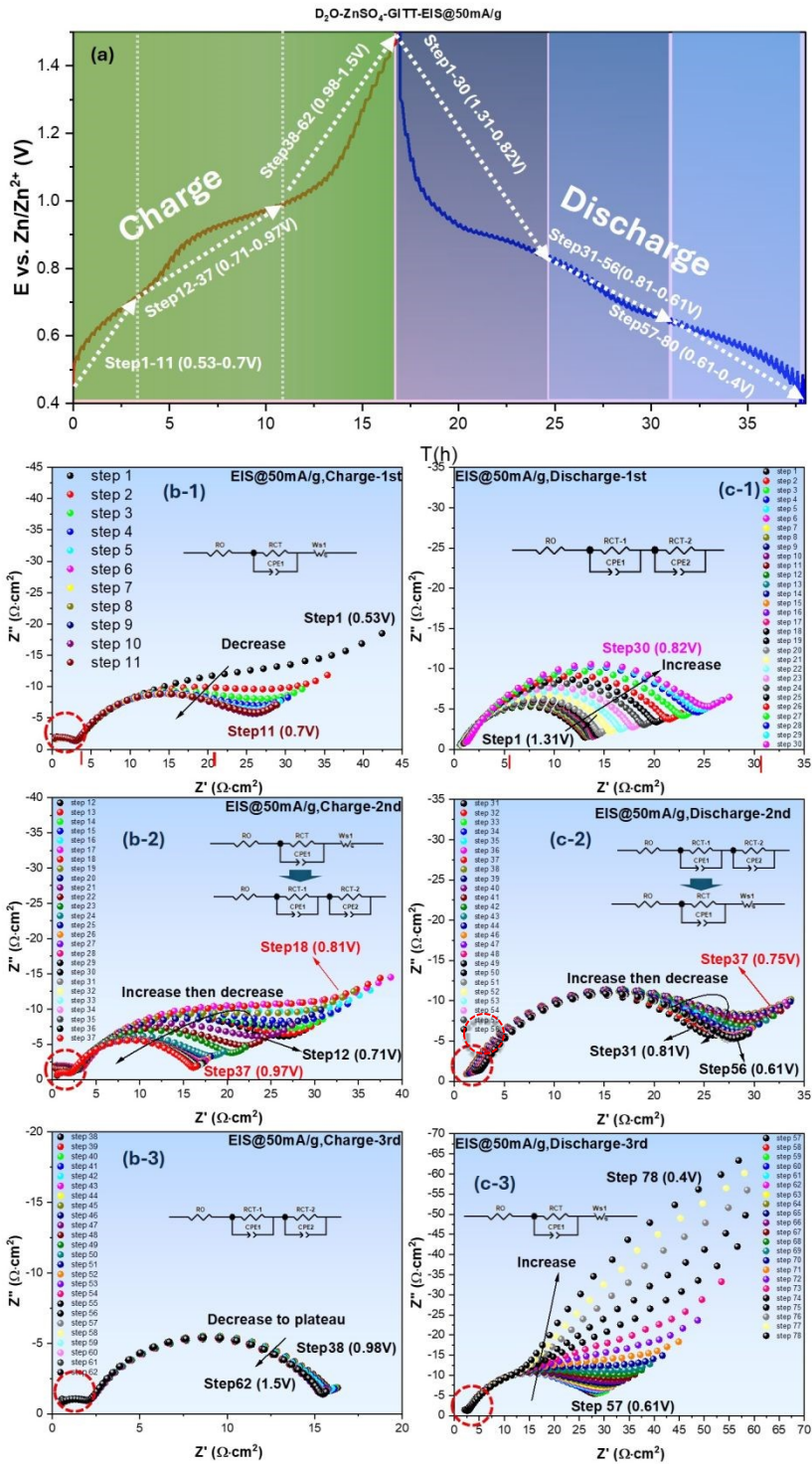


Figure 7. D₂O-ZnSO₄ system: (a) E vs. time profile collected under ± 50 mA/g; EIS spectra measured with ± 50 mA/g bias during (b) charge and (c) discharge cycles. Red circles mark the extra semicircle at high frequency range.

A noticeable difference of EIS spectra of the D₂O-ZnSO₄ system from H₂O-ZnSO₄ system, see Figure 7(b), is the appearance of a high-frequency semicircle (highlighted by red dotted circles) during the charge cycle. The magnitude of this small semicircle does not seem to change appreciably with SOC. Since D⁺ extraction from NaCaVO occurs during the charge cycle, the appeared semicircle (an extra charge transfer process) implies a reduced D⁺ extraction kinetics, which leads to a more sluggish V³⁺→V⁴⁺ redox reaction and increased relaxation time constant. Another notable observation is that the Warburg impedance becomes less pronounced as E increases, the same trend as the H₂O-ZnSO₄ system.

For the subsequent discharge cycle, see Figure 7(c), the EIS collected under high E (Figure 7(c-1), step 1-19, 1.5-0.83 V) show a much less pronounced, small high-frequency semicircle than that observed during the charge cycle. As E decreases, see Figure 7(c-2) (steps 20-39, 0.82-0.66 V) and (c-3) (steps 40-56, 0.65-0.4 V), this small high-frequency semicircle appears to increase slightly, while the Warburg impedance becomes more pronounced, like the H₂O-ZnSO₄ system. A comparison of EIS spectra vs. SOC between the H₂O-ZnSO₄ and D₂O-ZnSO₄ systems suggests similar charge transfer mechanisms, but the heavier D⁺ is more difficult to extract from the cathode, thus increasing the relaxation time constant of the process and depicting itself on the EIS spectrum within the frequency range studied. Since D₂O has the most pronounced impact on R_{CT} at low E, it is reasonable to speculate that H⁺/D⁺ (de)insertion into the cathode leads to the V³⁺⇌V⁴⁺ redox reaction.



To better illustrate how R_{CT} vary with SOC, we plot R_{CT} vs. E under different current densities in Figure 8. In general, the overall trend of each curve resembles Figure 3 of the $H_2O-ZnSO_4$ system, *i.e.*, they can be divided into three stages, featuring monotonically decreasing, peaking and flattening of R_{CT} with SOC. However, the magnitude of R_{CT} for the $V^{3+} \rightleftharpoons V^{4+}$ is significantly higher (by nearly 2 \times) in the $D_2O-ZnSO_4$ system than the $H_2O-ZnSO_4$ counterpart, whereas R_{CT} of the $V^{4+} \rightleftharpoons V^{5+}$ is close for the two electrolyte systems. This observation further supports the assertion that it is H^+/D^+ that are mainly responsible for the $V^{3+} \rightleftharpoons V^{4+}$ redox reaction.

The dependence of R_{CT} and η on the applied current density for the $D_2O-ZnSO_4$ system is plotted in Figure 9(a) and (b), where R_{CT} for the charge and discharge cycle at high E is seen to remain close but notably different at lower E , *i.e.* R_{CT} during the charge is lower than the discharge at a given SOC, which is like the $H_2O-ZnSO_4$ system.

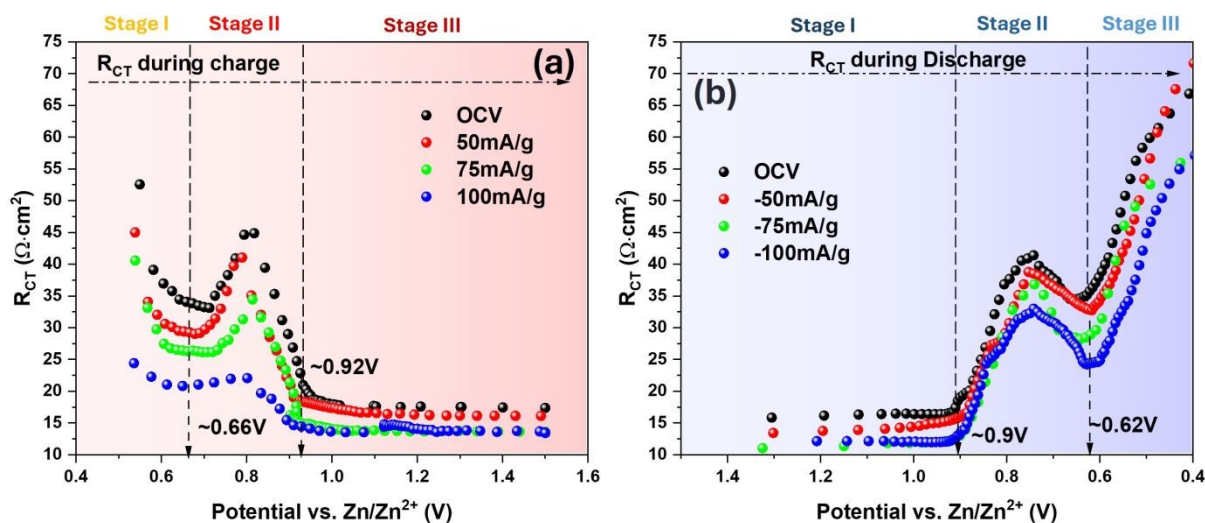


Figure 8. $D_2O-ZnSO_4$ system: R_{CT} vs. E during (a) charge and (b) discharge cycle under different current densities.



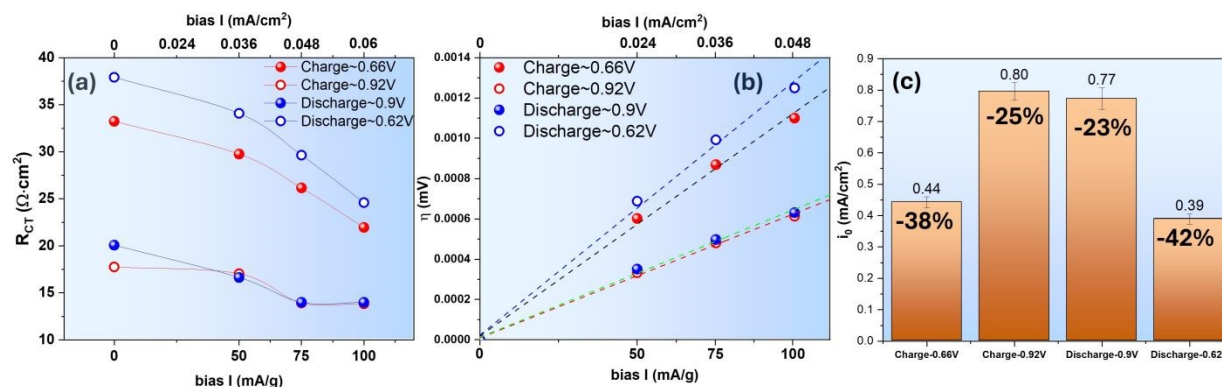


Figure 9. D₂O-ZnSO₄ system: (a) R_{CT} vs. i ; (b) η vs. i and (c) i_0 at 0.66 V and 0.92 V during charge and 0.90 V and 0.62V during discharge, with relative percentage of decrease compared to the H₂O-ZnSO₄ system.

Using the “low-field” approximation, the obtained i_0 of the D₂O-ZnSO₄ system is shown in Figure 9(c). The results indicate a greater decrease in i_0 than the H₂O-ZnSO₄ system, i.e., it is -38% and -42% for the charge and discharge cycle, respectively, for the $V^{3+} \rightleftharpoons V^{4+}$ occurring at low E and it is -25% and -23% for the charge and discharge cycle, respectively, for the $V^{4+} \rightleftharpoons V^{5+}$ occurring at high E. Such an increased difference could be attributed to the slower D⁺ (de)insertion kinetics than H⁺.

III. Conclusions

By applying a combined GITT-EIS approach, we quantitatively characterized the electrokinetics of NaCaVO cathode in AZIBs for the first time. Analysis of the charge transfer resistance (R_{CT}) and exchange current density (i_0) reveals that the $V^{3+} \rightleftharpoons V^{4+}$ redox reaction, which occurs at lower potentials during cycling, is intrinsically more sluggish than the $V^{4+} \rightleftharpoons V^{5+}$ counterpart at higher potentials. This difference is likely attributed to two possible factors: (1) a higher energy barrier for charge transfer at a deeper SOC, and/or (2) the formation of an intermediate Zn-LDH phase induced by the H⁺ insertion. The possibility of H⁺ insertion into the NaCaVO structure is further



supported by XRD and XPS analyses, as well as by the observed increase in R_{CT} upon replacing solvent H_2O with D_2O in the electrolyte. Since H^+ insertion into oxide-based cathodes is inevitable, the resultant Zn-LDH formation can also be viewed as an alternative way of Zn-ion storage. Overall, this study provides important fundamental insights into ion storage mechanisms in V_2O_5 -based cathodes and offers electrokinetic parameters for future computational modeling of AZIB systems.

Experimental Methods

Cathode synthesis and ink preparation

The NaCaVO cathode is synthesized using a hydrothermal method we developed previously.³⁶ Briefly, VCl_3 and $Ca(NO_3)_2 \cdot 6H_2O$ are mixed in deionized water with the pH adjusted to 7. The solution is then thermally treated at $190^\circ C$ for 24 hours in an autoclave, followed by washing and drying the solid precipitates at $60^\circ C$ for 12 hours. The synthesized material is characterized using X-ray diffraction (XRD) to confirm phase purity.

NaCaVO cathode ink is prepared by thoroughly mixing 66 wt% NaCaVO with 20 wt% Super-P and 14 wt% polyvinylidene fluoride (PVDF) in *N*-methyl pyrrolidone (NMP) solvent. The resultant slurry is then coated uniformly onto $\phi 10$ mm stainless steel meshes with ~ 0.6 $mg \cdot cm^{-2}$ active mass loading, followed by vacuum drying at $120^\circ C$ for about 12 h and compression under 10 MPa. The aqueous H_2O - $ZnSO_4$ and D_2O - $ZnSO_4$ electrolytes are prepared by dissolving 2M $ZnSO_4 \cdot 7H_2O$ (Sigma-Aldrich, ACS reagent, 99%) in DI water and D_2O (Sigma-Aldrich, 99.9 atom% D), respectively.

Electrochemical measurements



In this study, a 3-electrode electrochemical cell is constructed to characterize electrochemical behaviors of the NaCaVO cathode,⁵¹ in which NaCaVO is used as the WE, a zinc metal as CE, an Ag/AgCl as RE, and 2M ZnSO₄ as the electrolyte. During the measurement, Cyclic Voltammetry (CV) is first performed at different scanning rates (mV/s) to determine the number of redox reactions and their respective potentials. Once the redox potential is determined, we then cycle the NaCaVO-Zn 3-electrode cell 5 times from 1.5 V to 0.4 V vs. Zn/Zn²⁺ at 0.2A/g to fully activate the cathode. We then perform stepwise GITT-EIS measurements within a voltage window of 1.5 V and 0.4 V vs. Zn/Zn²⁺ to simulate charge and discharge cycles. Each GITT-EIS run consists of three phases. Phase-1: a ten-minute constant current polarization at 50 mA/g, either positive (charge) or negative (discharge), is applied to mockup galvanic charge/discharge operation in a battery; this operation creates many potential intervals representing different SOC_s (see later Figure 2(a)). Phase-2: EIS measurements are carried out right after the galvanic interruption under OCV as well as DC bias current in the range of ±50 to ±125 mA/g in step of ±25 mA/g within a frequency range of 1M Hz to 1 Hz with a base AC amplitude of 1 mA. The DC bias current is superimposed on the AC signal. Phase-3: there is a 1-minute resting period under OCV between each bias current. From the measured EIS spectra, R_{CT} under different bias are obtained using equivalent circuits. The obtained R_{CT} - i relationship is then used to attain overpotential (η) - i through integration, from which i_0 of NaCaVO at a specific potential can be obtained from the “low-field” approximation of Butler-Volmer equation given the low current density range used in this study. In addition, we also use DRT method to help analyze EIS data and facilitate the identification of elementary steps.

To illustrate the phase compositions and the variations of V-oxidation state with SOC_s, we employ XRD and XPS, respectively, to examine NaCaVO cycled at high voltage range (1.5 -



0.75 V at 0.2 A/g for 50 cycles) and low voltage range (0.75 - 0.4 V at 0.2 A/g for 50 cycles). The cycled samples are thoroughly rinsed with DI water before examinations to avoid interference from the electrolyte.

Materials characterization

The XRD is performed on fresh and post-tested NaCaVO samples using a Rigaku D/MAX-2100 with Cu K α radiation ($\lambda = 1.5418 \text{ \AA}$). The data are recorded from 5 to 80° with an interval of 0.02° and a scan speed of 2° min⁻¹.

The surface oxidation states of the sample are investigated with AXIS Ultra DLD XPS (Kratos Analytical) instrument. The XPS system is equipped with a non-monochromatic Al K α source (1486.8 eV) operated at 150 W X-Ray gun power, a hemispherical analyzer and a load lock chamber for rapid introduction of samples without breaking vacuum. The X-rays were incident at an angle of 45°, with respect to the surface normal. Analysis was performed at a pressure of $\sim 1 \times 10^{-9}$ Torr and high-resolution core level spectra were acquired in the constant analyzer energy mode using a pass energy of 10 eV and a 0.07 eV step size (for survey scans 80 eV pass energy is used with 0.08 eV step size). The XPS experiments were performed by using a low energy electron beam, directed at the sample, for charge neutralization. The Binding energies (BE) of all peaks are corrected in reference to the C 1s peak at 285 eV and given with an accuracy of ± 0.2 eV. The curve fitting procedure was carried out using the Advantage software.

Acknowledgement

This research was sponsored by the U.S. Army Research Office (ARO) and was accomplished under Grant Number W911NF-21-1-0308 and the U.S. Air Force Office of Scientific Research under Grant Number FA9550-23-1-0505. The views and conclusions in this document are those



of the authors and should not be interpreted as representing the official policies, either expressed or implied, of ARO or AFOSR or the U.S. Government. The U.S. Government is authorized to reproduce and distribute reprints for Government purposes, notwithstanding any copyright notation herein. The XPS facility receives financial support from the Office of the Vice President for Research, University of South Carolina.

References

1. G. Li, L. Sun, S. Zhang, C. Zhang, H. Jin, K. Davey, G. Liang, S. Liu, J. Mao and Z. Guo, *Advanced Functional Materials*, 2024, **34**, 2301291.
2. S. W. Gourley, R. Brown, B. D. Adams and D. Higgins, *Joule*, 2023, **7**, 1415-1436.
3. M. Armand and J.-M. Tarascon, *nature*, 2008, **451**, 652-657.
4. B. Dunn, H. Kamath and J.-M. Tarascon, *Science*, 2011, **334**, 928-935.
5. Z. Yang, J. Zhang, M. C. Kintner-Meyer, X. Lu, D. Choi, J. P. Lemmon and J. Liu, *Chemical reviews*, 2011, **111**, 3577-3613.
6. C. Xia, J. Guo, P. Li, X. Zhang and H. N. Alshareef, *Angewandte Chemie*, 2018, **130**, 4007-4012.
7. K. Zhu, T. Wu, S. Sun, Y. Wen and K. Huang, *ChemElectroChem*, 2020, **7**, 2714-2734.
8. K. Zhu, T. Wu, W. van den Bergh, M. Stefik and K. Huang, *ACS nano*, 2021, **15**, 10678-10688.
9. Y. Lu, T. Zhu, W. van den Bergh, M. Stefik and K. Huang, *Angewandte Chemie International Edition*, 2020, **59**, 17004-17011.
10. K. Zhu, T. Wu, S. Sun, W. van den Bergh, M. Stefik and K. Huang, *Energy Storage Materials*, 2020, **29**, 60-70.
11. J. J. Ye, P. H. Li, Z. Hou, W. Zhang, W. Zhu, S. Jin and H. Ji, *Angewandte Chemie*, 2024, **136**, e202410900.
12. C. Geng, P. Zhang, J.-M. Wu, J. Qin and W. Wen, *ACS nano*, 2024, **18**, 33119-33130.
13. W. Sun, F. Wang, S. Hou, C. Yang, X. Fan, Z. Ma, T. Gao, F. Han, R. Hu and M. Zhu, *Journal of the American Chemical Society*, 2017, **139**, 9775-9778.
14. X. Gao, H. Wu, W. Li, Y. Tian, Y. Zhang, H. Wu, L. Yang, G. Zou, H. Hou and X. Ji, *Small*, 2020, **16**, 1905842.
15. B. Zhang, P. Dong, S. Yuan, Y. Zhang, Y. Zhang and Y. Wang, *Chem & Bio Engineering*, 2024, **1**, 113-132.
16. D. S. Liu, Z. Zhang, Y. Zhang, M. Ye, S. Huang, S. You, Z. Du, J. He, Z. Wen and Y. Tang, *Angewandte Chemie International Edition*, 2023, **62**, e202215385.
17. B. Tang, L. Shan, S. Liang and J. Zhou, *Energy & Environmental Science*, 2019, **12**, 3288-3304.
18. S. Zuo, X. Xu, S. Ji, Z. Wang, Z. Liu and J. Liu, *Chemistry-A European Journal*, 2021, **27**, 830-860.
19. B. Yong, D. Ma, Y. Wang, H. Mi, C. He and P. Zhang, *Advanced Energy Materials*, 2020, **10**, 2002354.
20. Y. Lu, T. Zhu, W. van den Bergh, M. Stefik and K. Huang, *Angewandte Chemie*, 2020, **132**, 17152-17159.
21. V. Mathew, B. Sambandam, S. Kim, S. Kim, S. Park, S. Lee, M. H. Alfaruqi, V. Soundharrajan, S. Islam and D. Y. Putro, *ACS Energy Letters*, 2020, **5**, 2376-2400.
22. X. Gao, H. Dong, C. Su, Y. Dai, Y. Liu, I. P. Parkin, C. J. Carmalt, G. J. E. He, *Energy Environmental Science*, 2025, **18**, 13-18.



23. X. Li, J. Xiang, L. Qiu, X. Chen, Y. Zhao, Y. Wang, Q. Yue, T. Gao, W. Liu and D. Xiao, *Journal of Energy Chemistry*, 2025, **100**, 770-778.
24. P. He, G. Zhang, X. Liao, M. Yan, X. Xu, Q. An, J. Liu and L. Mai, *Advanced Energy Materials*, 2018, **8**, 1702463.
25. Y. Yang, Y. Tang, G. Fang, L. Shan, J. Guo, W. Zhang, C. Wang, L. Wang, J. Zhou and S. Liang, *Energy Environmental Science*, 2018, **11**, 3157-3162.
26. C. Liu, Z. Neale, J. Zheng, X. Jia, J. Huang, M. Yan, M. Tian, M. Wang, J. Yang and G. Cao, *Energy Environmental Science*, 2019, **12**, 2273-2285.
27. C. Xia, J. Guo, P. Li, X. Zhang and H. N. Alshareef, *Angewandte Chemie International Edition*, 2018, **130**, 4007-4012.
28. F. Ming, H. Liang, Y. Lei, S. Kandambeth, M. Eddaoudi and H. N. Alshareef, *ACS Energy Letters*, 2018, **3**, 2602-2609.
29. T. Lv, G. Zhu, S. Dong, Q. Kong, Y. Peng, S. Jiang, G. Zhang, Z. Yang, S. Yang and X. Dong, *Angewandte Chemie International Edition*, 2023, **135**, e202216089.
30. Y. Tan, F. An, Y. Liu, S. Li, P. He, N. Zhang, P. Li and X. Qu, *Journal of Power Sources*, 2021, **492**, 229655.
31. W. Weppner and R. A. J. Huggins, *Journal of The Electrochemical Society*, 1977, **124**, 1569.
32. E. Deiss, *Electrochimica Acta*, 2002, **47**, 4027-4034.
33. S.-I. Pyun and J.-S. Bae, *Electrochimica Acta*, 1996, **41**, 919-925.
34. X. Chen, L. Wang, H. Li, F. Cheng and J. Chen, *Journal of Energy Chemistry*, 2019, **38**, 20-25.
35. B. E. J. Conway, *Journal of The Electrochemical Society*, 1991, **138**, 1539.
36. K. Zhu, T. Wu and K. Huang, *Advanced Energy Materials*, 2019, **9**, 1901968.
37. N. Zhang, Y. Dong, M. Jia, X. Bian, Y. Wang, M. Qiu, J. Xu, Y. Liu, L. Jiao and F. Cheng, *ACS Energy Letters*, 2018, **3**, 1366-1372.
38. M. Yan, P. He, Y. Chen, S. Wang, Q. Wei, K. Zhao, X. Xu, Q. An, Y. Shuang and Y. Shao, *Advanced Materials*, 2018, **30**, 1703725.
39. S. Deng, Z. Yuan, Z. Tie, C. Wang, L. Song and Z. Niu, *Angewandte Chemie International Edition*, 2020, **59**, 22002-22006.
40. J. Kim, S. H. Lee, C. Park, H. S. Kim, J. H. Park, K. Y. Chung and H. Ahn, *Advanced Functional Materials*, 2021, **31**, 2100005.
41. J. Ding, Z. Du, B. Li, L. Wang, S. Wang, Y. Gong and S. Yang, *Advanced Materials* 2019, **31**, 1904369.
42. A. J. Bard, L. R. Faulkner and H. S. White, *Electrochemical methods: fundamentals and applications*, John Wiley & Sons, 2022.
43. B. He, Y. Ling, Z. Wang, W. Gong, Z. Wang, Y. Liu, T. Zhou, T. Xiong, S. Wang and Y. Wang, *eScience*, 2024, **4**, 100293.
44. T. F. Fuller and J. N. Harb, *Electrochemical engineering*, John Wiley & Sons, 2018.
45. T. H. Wan, M. Saccoccio, C. Chen and F. Ciucci, *Electrochimica Acta*, 2015, **184**, 483-499.
46. Z. Li, S. Ganapathy, Y. Xu, Z. Zhou, M. Sarilar and M. Wagemaker, *Advanced Energy Materials*, 2019, **9**, 1900237.
47. A. Macrelli, M. Olivieri, A. Lamperti, V. Russo, B. Bozzini, M. Menegazzo, G. Bussetti, C. S. Casari and A. L. Bassi, *Electrochimica Acta*, 2023, **442**, 141909.
48. M. Liu, Z. Li and Y. Zhang, *Journal of Electroanalytical Chemistry*, 2023, **942**, 117539.
49. F. Gong, Y. Feng, Y.-H. Fang, Y.-K. Hsu, and Y.-C. Chen, *ACS Applied Materials Interfaces*, 2023, **15**, 18808-18818.
50. D. Zhang, J. Cao, Y. Yue, T. Pakornchote, T. Bovornratanaraks, J. Han, X. Zhang, J. Qin, and Y. Huang, *ACS Applied Materials Interfaces*, 2021, **13**, 38416-38424.
51. S. Sun, A. Billings, B. Wang and K. Huang, *ACS electrochemistry*, 2024.



Data Availability Statement

The data supporting this article have been included as part of the Supplementary Information.

